The complex basal morphology and ice dynamics of Nansen Ice Shelf, East Antarctica

Christine F. Dow[1], Derek Mueller[2], Peter Wray[1], Drew Friedrichs[3,4], Alexander L. Forrest[3,4], Jasmin B. McInerney[3,4], Jamin Greenbaum[5], Donald D. Blankenship[6], Choon Ki Lee[7], Won Sang Lee[7]

[1]Department of Geography and Environmental Management, University of Waterloo, Waterloo, Canada, N2L 3G1
[2]Department of Geography and Environmental Studies, Carleton University, Ottawa, Canada, K1S 5B6
[3]Department of Civil and Environmental Engineering, University of California – Davis, Davis, USA, 95616
[4]Tahoe Environmental Research Center, University of California – Davis, Incline Village, USA, 89451
[5]Scripps Institution of Oceanography, University of California, San Diego, La Jolla, CA, USA
[6]Institute for Geophysics, Jackson School of Geosciences, University of Texas at Austin, Austin, TX, USA, 78758
[7]Division of Glacial Environment Research, Korea Polar Research Institute, Incheon 21990, Republic of Korea

Correspondence to: Christine F. Dow (christine.dow@uwaterloo.ca)

Abstract. Ice shelf dynamics and morphology play an important role in the stability of floating bodies of ice, in turn impacting their ability to buttress upstream grounded ice. We use a combination of satellite-derived data, airborne and ground-based radar data, and oceanographic data collected at the Nansen Ice Shelf in East Antarctica to examine the spatial variations in ice shelf draft, the cause and effects of ice shelf strain rates, and the role of a suture zone driving channelization of ocean water and resulting sub-ice shelf melt and freeze-on. We also use the datasets to assess limitations that may arise from examining only a sub-set of the data, in particular the reliance on hydrostatic balance equations applied to surface digital elevation models to determine ice draft morphology. We find that the Nansen Ice Shelf has highly variable basal morphology driven primarily by the formation of basal crevasses near the onset of floating ice convergence in the suture zone. This complex morphology is reflected in the ice shelf strain rates but not in the calculated hydrostatic balance thickness, which underestimates the scale of vertical and horizontal variability at the ice shelf base. The combination of thinner ice in the channelized suture zone, enhanced melt rates near the ice shelf edge, and complex strain rates driven by ice dynamics and morphology have led to the formation of fractures within the suture zone that have resulted in large-scale calving events. Other Antarctic ice shelves may also have complex morphology, which is not reflected in the satellite data, yet may influence their stability.

1 Introduction

Ice shelves play an important role in buttressing large portions of the Antarctic Ice Sheet, preventing destabilization of grounded ice and related discharge into the ocean (Dupont and Alley, 2005; Fürst et al, 2016; Scambos et al, 2014). The stability of these ice shelves is therefore vital for determining the future rise of global sea level. Fracturing and calving is a key process in the evolution of ice shelf morphology and its ability to hold back grounded ice. Ice shelf fractures occur in regions that are undergoing stress greater than the cohesive strength of the ice and can form or expand as a result of flexure (Vaughan et al, 2012); longitudinal stretching as ice moves beyond pinning points (Dow et al, 2018; Indrigo et al, 2020); advection of crevasses from grounded ice across the grounding line (Kulessa et al, 2014); and changes in buttressing causing ice shelf acceleration (Fürst et al, 2016). The primary controls of fracture formation include the ice thickness, the ice strain regime, and the ice rheology, along with additional factors such as the stress intensity factor (Lipovsky, 2018).

It is possible to predict the response of a flat body of floating ice to warming atmospheric and ocean conditions but, in reality, ice shelves consist of complex morphology and rheology making it a challenge to determine potential fracture and/or

break-up locations. The increasing availability of high-resolution data products such as ice velocity (e.g. Global Land Ice Velocity Extraction from Landsat 8 (GoLIVE) project; Scambos et al., 2016), and ice surface elevation (e.g. the Reference Elevation Model of Antarctica (REMA, Howat et al, 2019)) open up possibilities for large-scale spatial analyses of ice shelf processes. However, the use of inferred data (e.g. assumptions of hydrostatic equilibrium for floating ice bodies) may

45   obfuscate ice shelf morphological details and lead to misconceptions regarding important processes and properties.

Here we use the Nansen Ice Shelf (NIS) in Terra Nova Bay as a case study to examine the cause of complex ice shelf morphology; its implications for ice rheology, strength and potential to fracture; along with the applicability of different data types for ice shelf analysis. The NIS is a cold-cavity ice shelf and has a thin suture zone where a transverse fracture formed

50   around 1987, advected towards the ice shelf terminus while expanding laterally, and resulted in a large (213 km^2 in ice extent) calving event in 2016 (Dow et al, 2018). Around the time of this event, the ice surface strain patterns changed from extensional across-ice to extensional down-ice within ~8 km of the calving front and drove the formation of a new fracture over the thinnest region of the central NIS. This ice shelf is therefore an interesting test case for examining how interactions between ice shelf morphology and strain in thin-ice regions may enhance stress and cause fracturing.

55

We analyze and compare several datasets including a satellite-derived digital elevation model (DEM), ground-based and airborne ice-penetrating radar (IPR), ice velocity-derived strain rate data, and oceanographic data. These data sets are used to examine the morphology of NIS and how this interacts with ice rheology and ice strain, both important factors in shelf fracturing. By comparing and combining these satellite and *in situ* data we make recommendations of where and when

60   satellite data is sufficient to analyse ice shelf properties without *in situ* data.

2. Site Description

The NIS, with an area of ~1800 km^2, is located in Terra Nova Bay and is part of the Victoria Land Coast of the Western Ross Sea region in East Antarctica. The two primary glaciers that supply the NIS are the Reeves Glacier to the south and the Priestley Glacier to the north (Fig. 1a). The Priestley Glacier is more than 1000 m thick near its grounding line and has ice

65   surface velocities up to 130 m a^{-1}, with an estimated ice discharge of 0.77 ± 0.13 km^3 a^{-1} (Frezzotti et al., 2000). The Reeves Glacier separates into two distinct branches as it flows around the Teall Nunatak and down a substantial ice fall at its grounding line. The Reeves Glacier is ~700 m thick at its grounding line with an average surface ice velocity of 200 m a^{-1} and an approximate ice discharge of 0.52 ± 0.06 km^3 a^{-1} (Frezzotti et al., 2000). The grounding lines of the Priestley and Reeves glaciers have been estimated to be 70 km and 40 km from the ice shelf terminus, respectively (Mouginot et al. 2017),

70   and the floating ice from these glaciers converges ~ 30 km from the ice shelf terminus in a suture zone. Inexpressible Island is a small land mass and pinning point located at the north-eastern end of the ice shelf terminus dividing the main NIS from the smaller Hell's Gate Ice Shelf.

The NIS ranges in thickness from 1000 m at the Priestley Glacier grounding line to 120 m at the ice shelf terminus. A 30 km-long surface depression runs east-west across the NIS along the suture zone of the Reeves and Priestly glacier branches

75   (Alley et al., 2016; Bell et al., 2017, Baroni et al., 1991; Dow et al., 2018). A river was observed in the surface depression as early as 1974 and annually from 2014-2016 (Bell et al., 2017). During the melt seasons of 2014-2016 the river flowed into the transverse fracture prior to the calving event in April 2016 (Dow et al., 2018). The katabatic winds that allow persistence of a significant polynya at the terminus of the NIS also strips the ice shelf of much of its snow and firn cover leaving a significant portion of the surface as blue ice (Kurtz and Bromwich, 1983). The polynya plays an important role in sea ice

80   production for the Ross Sea (Stevens et al., 2017).
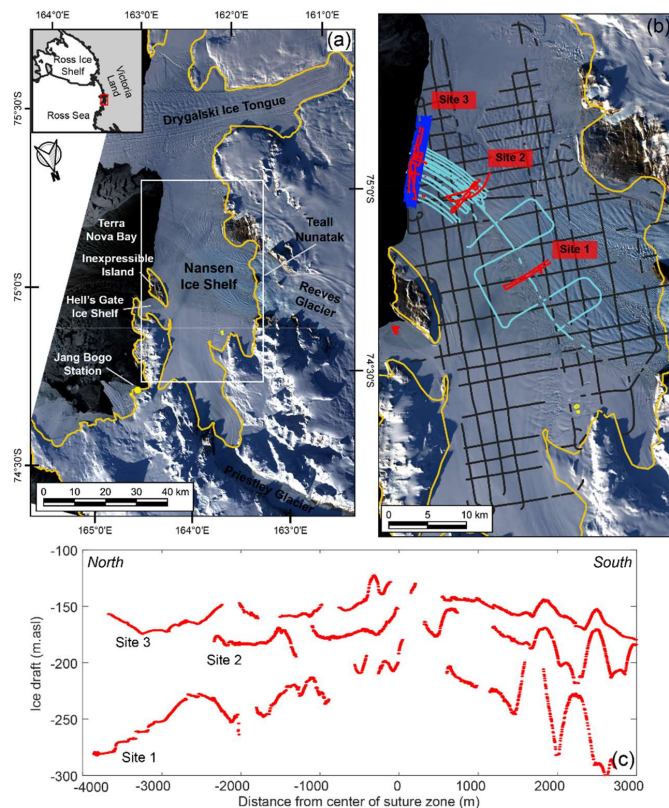
Figure 1: Site map with radar lines and cross sections. a) The Nansen Ice Shelf (NIS) and grounding line/coastline (yellow line) from MEaSUREs Antarctic Boundaries v2 (Mouginot et al., 2017) on a background image from Landsat-8 acquired March 22, 2017. Inset: Victoria Land and western Ross Sea region, red box is the location of the NIS. b) Ground-based ice-penetrating radar (IPR) lines at sites 1,2 and 3 from November 2016 (red), Airborne IPR survey from January 2017 focused on the ice shelf front (dark blue) and suture zone (cyan), Airborne IPR survey from January 2017 of the entire NIS (black). c) Three ice draft lines, one from each site. The location of these transects are shown in Fig. 2a.

3 Methods

3.1 Ice penetrating radar

Between November 3-19 2016, ~80 km of ground-based ice penetrating radar (IPR) surveys were conducted on foot at three targeted sites focused on the suture zone of the NIS resulting in an trace separation of ~1 m (see Appendix A), later down-sampled to a separation of 4 m. Some locations lacked a bed reflection, especially at Site 3 closest to the terminus, and repeat surveys verified that it was location specific.

In addition to the concentrated ground-based radar surveys, a helicopter-based airborne geophysical survey was based out of the South Korean Jang Bogo Station between December 25 2016 and February 18 2017 (Lindzey et al., 2020; see Appendix A). In total, 1000 km of surveys were conducted over the NIS in both a grid-pattern and concentrated over the suture zone near the ice shelf terminus (Fig. 1 a,b). An error analysis was conducted using the cross-over surface elevations and ice thickness of both the ground-based and airborne radar and is detailed in the Supplementary materials.

100 **3.2 Digital Elevation Maps**

Although the radar data provide information on the ice thickness and draft in our focused sites on the NIS, it is sufficiently sparse that DEMs interpolated from these data have significant errors in regions that lack high data density. As an alternative, we amalgamated 2 m resolution Reference Elevation Model of Antarctica (REMA) strips (Howat et al, 2019) for the NIS (Fig. 2a). We used three strips spanning the period of April 17 2016 to November 9 2016 to overlap with our IPR

105 data collection period. Due to the seven-month time difference, there was a slight offset between the strips. We corrected these to the GLO04C geoid and applied hydrostatic calculations to invert for basal draft (*B*) (Fig 2b), using the equation:

$$B = S - \frac{S \cdot \rho_s}{(\rho_s - \rho_i)},\tag{1}$$

where S is the measured surface elevation above the GL04C geoid, ρ_s is the density of sea water (1028 kg m^{-3}) and ρ_i is the density of meteoric glacial ice (917 kg m^{-3}). The zone of firn-free blue ice covers the regions of ground-based radar survey

110 but firn is present towards the grounding line of Reeves Glacier and Inexpressible Island, so in these regions the hydrostatic calculations are less accurate. We lack information on the thickness of firn in these regions precluding the inclusion of different density profiles in our application of Eq. 1. Assuming a REMA surface elevation error of <1 m (Howat et al, 2019), the hydrostatic thickness in the firn-free region has an associated error of ± ~10 m. Additional sources of hydrostatic thickness error such as assumptions of ice density and bridging stresses will be discussed in section 4.6.
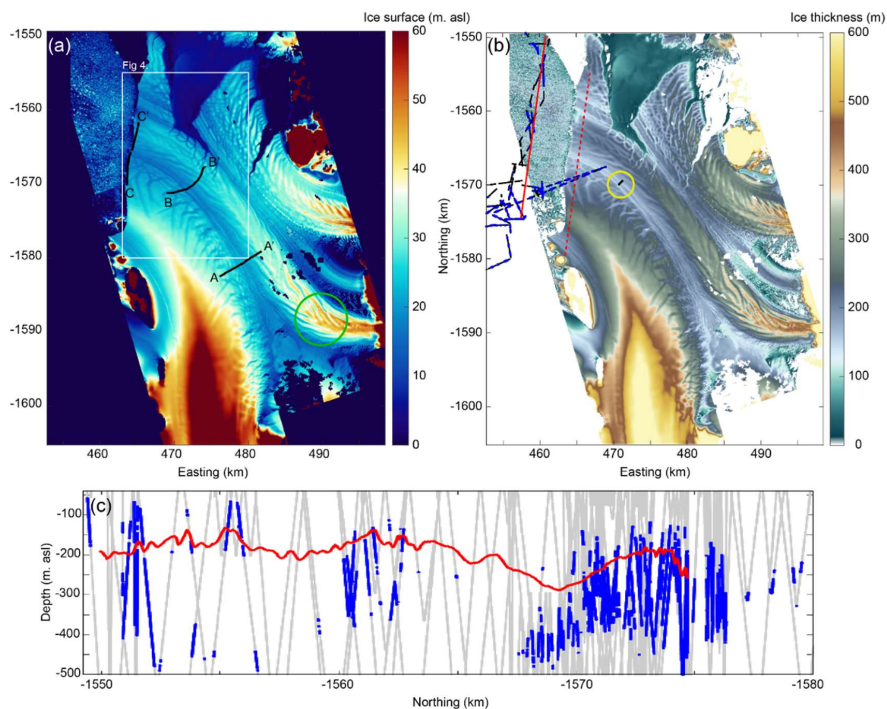
115

Figure 2: Nansen Ice Shelf DEMs a) REMA ice surface elevation with the three transects in Fig. 3 plotted in black. The extent of Fig. 4 is shown by the white box. The green circle highlights an area referenced in the text. b) Ice draft DEM from hydrostatic calculations applied to a) and assuming no firn. Blue points are the locations where meltwater was detected by the ocean glider with black points indicating all locations where glider data was collected between 40 and 500m depth. The

120 dashed red line shows the location of REMA hydrostatic ice draft plotted in c), adjusted to the downstream location of the glider data (solid red line). The black line highlighted by the yellow circle marks the location of a fracture first observed in

2016. c) Glider observations at intermediate depths (40-500 m) are indicated by grey lines. The locations of ice shelf meltwater are shown in blue. The solid red line indicates ice shelf draft from REMA hydrostatic inversions.

3.3 Fluxgate analysis

125 To assess the change in ice shelf shape in the suture zone as it advects downstream, we conducted a fluxgate analysis using cross-sections from radar and ice surface elevation transects, one from Site 1 (closest to the grounding line) and one from Site 3 (closest to the ice shelf edge), along with velocities at these sites extracted from the Landsat 8 derived GoLIVE database (Scambos et al., 2016). The velocity for Site 3 is extracted 500 m east of its true position as there is noise on the boundary pixels of the GoLIVE velocities between the ice shelf and the ocean. These lines are separated by ~22 km and, in

130 cross-section, common basal features are identifiable as apexes (thinner ice regions) and keels (thicker ice region, deeper in the ocean). Using these basal features, we chose boundaries (shown in Fig. 3a and c by the dashed lines) and calculated the flux using the following equation:

$$\emptyset = \int_a^b v(x)cos\alpha(x)H(x)dx \ , \qquad\qquad (2)$$

where v is the ice flow speed at transect position x, α is the angle between the velocity vector and the direction perpendicular

135 to the transect, and H is the ice thickness. Error in the flux gate calculation is determined by applying the radar thickness uncertainty discussed in Appendix A3.
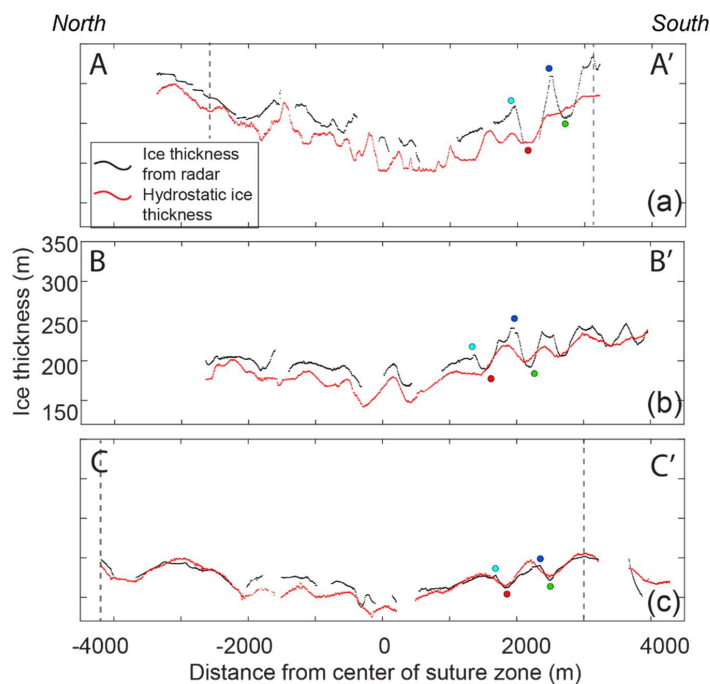
Figure 3: Cross-ice shelf transects of ice thickness from radar measurement (black) and from hydrostatic balance calculations using the ice shelf surface elevations (red) at a) Site 1, b) Site 2 and c) Site 3 on the Nansen Ice Shelf. The

140 colored dots represent where the basal draft apexes and keels were compared between sites. The dashed grey lines show the limits of the flux gate calculations. Transects are marked on Fig. 2.

3.4 Strain rates

NIS ice surface velocity data were obtained from GoLIVE. The closest nearly cloud-free period (September 29 – October 31, 2016) prior to the November 2016 IPR surveys was selected. The relationship between velocity vectors and vertical strain

145   rate on an ice shelf is related by conservation of mass:

$$\dot{\varepsilon}_1 = \dot{\varepsilon}_{xx} + \dot{\varepsilon}_{yy} + \dot{\varepsilon}_{zz} = 0, \tag{3}$$

where ε_1 is the net strain rate of the ice, which is equal to zero and $\dot{\varepsilon}_{xx}$, $\dot{\varepsilon}_{yy}$ and $\dot{\varepsilon}_{zz}$, are the strain rates parallel to principal x, y and, z axes respectively (Weertman, 1973). We reoriented the GoLIVE velocity vectors so that the x direction is transverse and the y direction is longitudinal (down-flow) to the ice shelf flow direction. We then calculated the principal

150   strain in the longitudinal and transverse directions using equations detailed in Dow et al (2018) with a length scale of 300 m, the pixel size of the GoLIVE velocity data. We ran a sensitivity test with a length scale of 600 m, which produced similar results in both spatial pattern and magnitude of strain rates. We interpolated the strain values from the 300 m length scale calculation to the radar data locations to assess the relationship between topography and ice surface strain on the NIS (Fig. 4).

155   ### 3.5 Ocean glider data

Between December 31, 2018 and January 10, 2019, a 1000 m depth rating G2 Slocum autonomous underwater glider was deployed along the NIS to collect observations of meltwater within the water column. Approximately 200 vertical profiles were completed across more than 100 km of transects back and forth along the ice shelf calving front, including ~10 km beneath the NIS, near the suture zone. Hydrographic measurements were recorded on the glider using a SeaBird SBE-41

160   CTD (conductivity-temperature-depth) sensor to infer the presence of meltwater. Other water column parameters were collected (e.g. dissolved oxygen, chlorophyll, turbidity, etc.) but will not be presented here.

4 Results

4.1 Nansen Ice Shelf morphology

165   Satellite products providing surface topography in the Antarctic are now high resolution (2 m horizontal from REMA) and provide excellent detail for analyses of surficial processes (Fig. 2). The suture zone between Reeves and Priestly glaciers is an area of thin ice driven by a limited supply from the glaciers that only converge once they are already floating. The lateral stretching as the glaciers converge likely plays a role in the limited thickness of the ice in this area (which is 200 m where they first join). The initial width of the thin-ice region in the suture zone where the glaciers first converge is ~4.5 km with a

170   difference in thickness of 50 m between the thin center of the suture zone and the thicker margin of the zone. Within 15 km of the calving front, the thin-ice region widens to 10 km with a draft difference of 90 m and 60 m, respectively, between the center of the suture zone and the northern and southern suture zone margins. At the terminus, the northern flank of the thin-ice region is wider (6 km) than the southern flank (4 km) with an average ice draft slope of ~1.3˚ and ~1.1˚ at the ice shelf terminus, respectively (Fig. 1c).

175

There is complex morphology consisting of multiple basal fractures, within the suture zone (Bell et al, 2017). These are discrete semi-continuous features that run parallel (on the southern side) or oblique (on the northern side) to the centre of the suture zone (Fig. 2). These basal features are altered as they advect downstream but we continue to refer to them as basal fractures for consistency (Fig. 2). The southern flank fractures are always parallel to the suture zone but are discontinuous

180   and range from 15 - 25 m in height with a width of ~500 m on average (as determined from our radar data; see Fig. 3). On

the northern flank, the features are also ~20 m high and ~500 m wide (Fig. 3) and are 3-5 km long near the ice shelf terminus (Fig. 2). In contrast to the southern features, these sweep away from the center of the suture zone to the north following a semi-circular pattern, and curve up to 90° from their original orientation. These basal fractures originate upstream in the respective floating margins of Priestley and Reeves ice, prior to their convergence in the suture zone.
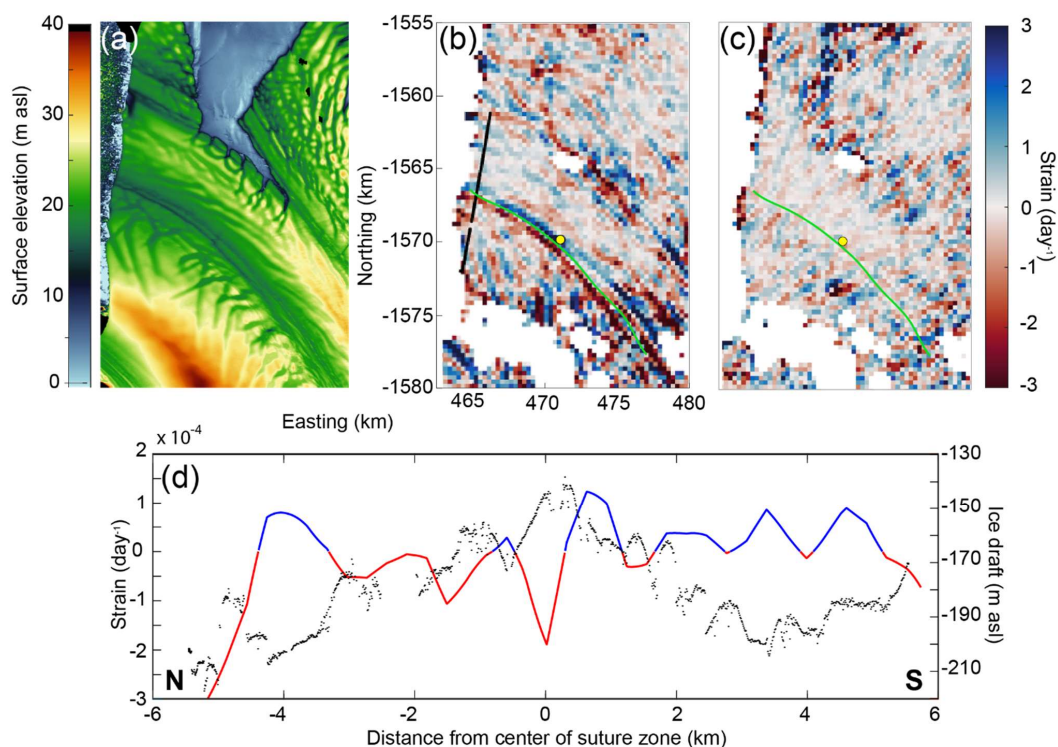
Figure 4: a) NIS REMA surface elevation composite. NIS ice surface a) transverse and b) longitudinal strain calculations from 2016 GoLIVE velocity data. Red areas show compression and blue areas show extension. The black line is the extent of the airborne radar transect shown in c). The green dashed line is the center of the suture zone and the yellow circle shows the 2016 fracture location. d) Profile of the radar transect showing ice shelf draft (black) and strain rate (red: compression; blue: extension) interpolated along the transect.

4.2 Strain rates

Some patterns of compressional and extensional transverse strain appear to be related to the suture zone features. We show horizontal transverse strain rates derived from 2016 GoLIVE ice surface velocity of the NIS (Fig. 4b) and a cross-section of strain rates plotted against the basal draft (Fig. 4d). The extent of the region in Fig. 4b is shown in Fig. 2. We note that the patterns of strain discussed here are also visible in NIS strain rate maps from multiple years, at different times of the year, and therefore appear to persist over time (e.g. see Fig. 5 in Dow et al, 2018).

Along the center of the suture zone there is an alternating region of horizontal compression (red) on the northern side and extension (blue) on the southern side: both regions have widths of ~800 m. When compared with the ice shelf draft, the switch between compression and extension occurs at the apex of the thin-ice suture zone region (Fig. 4d) and is limited horizontally where the ice thickness changes due to presence of the basal fracture keels. To the north, where the basal

fractures curve, there is compression at the apexes of the fractures and extension at the keels. The patterns of strain can be seen in the 2D map (Fig. 4b) as well as in the cross-section with the radar-derived basal draft (Fig. 4d).

On the southern side of the suture zone, the relationship between basal fractures and strain is less clear with compression in the apex of the first fracture at 1500 m from the center and again at 2800 m from the center at the apex of another fracture.

205   Otherwise, the strain is extensional. Similarly, in the 2D map, the strain patterns do not seem to align particularly well with the fractures on the Reeves side.

We also show the map of longitudinal strain rate in Fig 4c. The pattern and signal in the longitudinal strain rate is poorly resolved compared to the transverse strain rate in Fig. 4b. The transverse strain rate therefore appears to be the primary control on the patterned variability in extension and compression on the NIS.
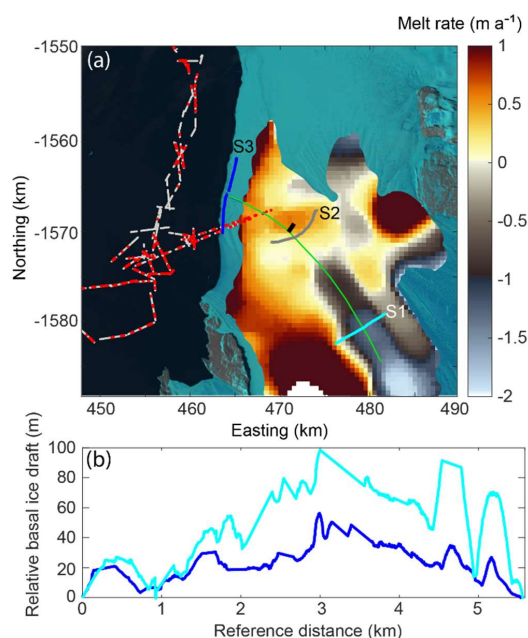
210

Figure 5: a) NIS melt rates averaged between 2010-2018 from Cryosat-2 data; data from Adusumilli et al. (2020). The 2016 fracture is plotted in black, and the site transects shown in Fig. 3 in cyan (Site 1), grey (Site 2) and blue (Site 3). Red points are the locations where ice shelf water was detected by the ocean glider instruments with grey points indicating all locations where glider data was collected between 40 and 500m depth. The center of the suture zone is shown in green. The

215   background is a Landsat-8 image acquired on January 2, 2019. b) Relative transverse change in basal draft for Site 1 (cyan) compared to Site 3 (blue). These are the radar lines used for flux gate analysis. The measured draft in m. asl. is shown in Fig. 1c.

4.3 Ice shelf melt rates

We aim to determine where mass loss or gain is occurring at this cold-cavity ice shelf. First, we perform a flux gate analysis

220   between two transects of the suture zone to assess how much mass loss occurs as the ice flows towards Terra Nova Bay. The discharge at Site 1 is 0.262 ± 0.004 km^3 a^{-1} and at Site 3 is 0.223 ± 0.005 km^3 a^{-1} demonstrating an average cross-sectional mass loss of 1740 ± 43 m^2 a^{-1} as the ice flows ~22 km between these two sites. It takes an average of 125.5 years for the NIS to flow over this distance using velocities extracted from GoLIVE. To examine where most of this mass loss is occurring, we

compare the horizontal difference in basal draft from the two sites directly (Fig. 5b). The northern side of the suture zone has
225   minimal change in relative basal draft but approaching the apex of the thin ice region, there is substantially more ice loss.
The greatest mass loss is in the highest apexes of the central suture zone and the basal fractures on the southern side, with the
keels of the latter relatively unchanged compared to the spatially-constant background melt rate. It is possible that mass loss
is due primarily to surface melt and sublimation, which was estimated by Bromwich and Kurtz (1984) to be 0.25 m a^{-1}.
However, the limited draft change at the margin of the northern part of the suture zone along with the presence of the Nansen
230   River, which focuses frictional melt into two narrow (<100 m wide) channels in the middle of the suture zone, suggests that
the change in basal draft is driven primarily by ocean processes such as accelerated buoyancy-driven flow where ice draft
slopes are steeper (Little et al, 2009).

We also estimate basal melt rate using the IPR data by examine ice draft thinning between Sites 1 and 3 using four clearly
identifiable keels and apexes in the ice draft in both locations. From these points, the vertical ice thickness change is 94 m
235   (keel, cyan point on Fig. 3a,c), ~57 m (apex estimated due to the lack of radar return at the tip of the ridge; red point) , 119 m
(keel; blue point), and 85 m (apex; green point). This translates to average vertical melt rates of 0.75 m a^{-1} (keel), 0.45 m a^{-1}
(apex), 0.95 m a^{-1} (keel), and 0.68 m a^{-1} (apex) between the two sites. However, as this is comparing different basal fracture
features rather than the same section of ice, the change in shape may be due to differences in initial fracture formation. We
therefore also compare these values to melt rates derived from Cryosat-2 satellite radar altimetry data provided as a grid with
240   500 m spatial resolution over the NIS (Fig. 5a; Adusumilli et al., 2020). The melt rates from Cryosat-2 indicate there are
regions of freeze-on (indicated by negative values) initiating where the suture zone begins with a maximum estimated mass
gain of ~2 ± 0.5 ma^{-1} (Fig. 5a). At Site 1, the maximum mass gain is 1.3 m a^{-1} ± 0.5 ma^{-1}. Within the suture zone, there is
then a transition into a region of melt 4 km upstream of Site 2. Site 2 itself is close to the maximum melt rate in the suture
zone of 0.6 m a^{-1} ± 0.5 ma^{-1}. The record does not cover Site 3 but the closest region has melt rates of ~1 ± 0.6 ma^{-1}, although
245   this may be unreliable due to the 2016 calving event which is within the window of altimetry data amalgamation.

4.4 Ice rheology

There were several regions on the NIS where the ice base horizon was not visible in the airborne and ground-based radar
record (Fig. 6 a,d). Given the abundance of clear ice base signals in the remainder of the radar data, it is likely that these
"echo-free zones" represent marine ice accumulation (Holland et al, 2009). Mapping these regions on top of the REMA 2016
250   hydrostatic thickness map shows they are all associated with thinner regions of ice and, in particular, with basal fractures on
both sides of the suture zone along with the thinnest portion of ice in the suture zone. On the ice surface, in the suture zone,
there are many stripes of clear blue ice between larger regions of white aerated ice (Fig. 6c). These can be traced back to the
Reeves Glacier ice fall where crevasses fully fracture through the ice column, fill with sea water and refreeze (Khazendar et
al, 2001). The filled crevasses are then advected and stretched, producing visible stripes parallel to the ice flow direction
255   along the suture zone. It was across one of these striped regions (where ice is among the thinnest in the suture zone) that a
new fracture was found during fieldwork in 2016 (Dow et al, 2018; see yellow circle in Fig. 2b).

4.5 Oceanography data

Terra Nova Bay seawater is notably colder (potential temperature ~-2.0 to -1.5 °C) and more saline (practical salinity values
ranging from ~34.70 to 34.85) in comparison to other Antarctic coastal waters. The dense deep water (potential density >
260   1028 kg m^{-3}) is presumed to drive basal melt (Rusciano et al., 2013), resulting in the formation of frigid ice shelf meltwater
(potential temperature < -1.94°C) at or below the point of supercooling. In the summer season, a layer of warm and fresh
surface water also develops in Terra Nova Bay that varies greatly in temperature (θ_T > +1.0 °C) and salinity (S < 34.55
PSU).

265 We plot the glider data representing the location of cold, fresh, ice shelf water on Figs. 2b, 5 and 1. This ice shelf meltwater was distributed along the NIS calving edge at intermediate depths, beneath the warm Summer Surface Water and above the deep High Salinity Shelf Water. There are three regions where this water appears: one is adjacent to Drygalski Ice Tongue and has meltwater at depths between 58-490 m; the second is towards the middle of the ice shelf with depths between 113-397 m; the third is close to Inexpressible Island at the northern margin of NIS and has depths between 128-502 m. Our IPR

270 data show that the draft of the NIS adjacent to the ice shelf water mass sitting mid-way along the NIS ranges from 150-190 m in depth. For the northern meltwater mass, the NIS draft ranges between ~160 and ~230 m depth (as determined from REMA hydrostatic calculations).
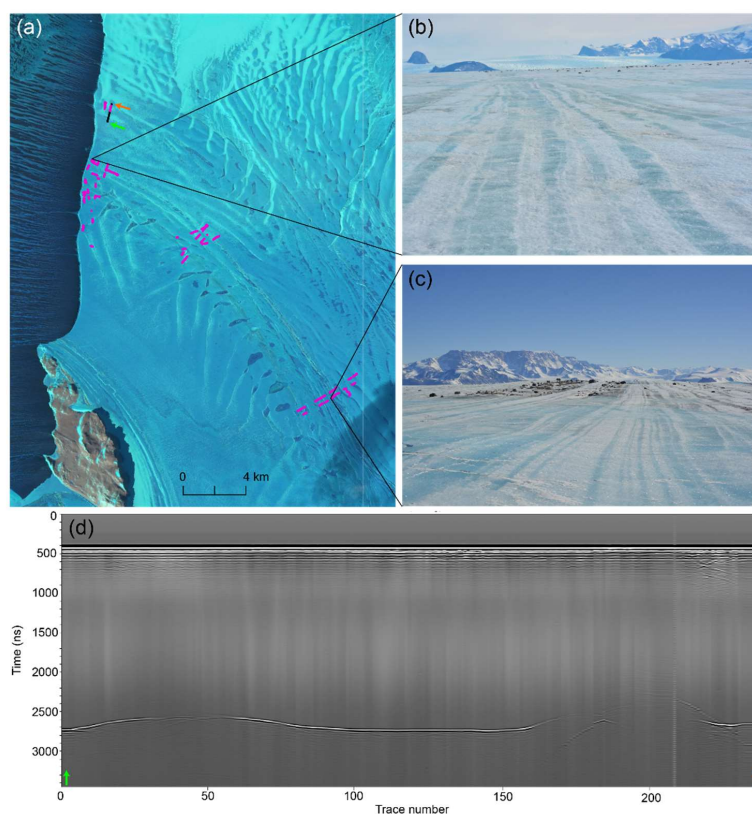
275 **Figure 6:** a) Sentinel image of NIS from October 5th 2016. Pink points are regions with radar signal dropout likely representing the presence of marine ice. The coloured arrows and the black line show the extent of the radar transect shown in d). b) and c) photos of surface striping on NIS showing filled crevasses associated with the marine ice drop-out regions taken on November 11 and November 18, 2016, respectively. d) Radargram with a gain of 0.5 and signal dropout between traces 170-220. The coloured arrows correspond to those in a).

280 **4.6 Hydrostatic equilibrium**

Satellite-derived estimations of ice shelf draft data are limited by assumptions of hydrostatic balance, which do not take bridging stresses or pinning points into account. Our *in situ* ground-based and airborne radar data provide high-resolution

data of ice shelf draft features and allow analysis of where the hydrostatic DEMs lose accuracy as well as how these features change as they advect downstream (e.g. Fricker et al, 2001).

285   In comparing ice thickness data from the IPR cross-sections with thickness derived from GNSS elevation and hydrostatic calculations we found that the best match is at Site 3 nearest to the terminus but at Site 1 and 2 further upstream there was a vertical offset where the ice thickness measured using the radar was greater, on average, than the ice thickness derived from surface altimetry (Fig. 3). On the southern side of the suture zone at Site 1 between ~2000-2500 m, the large variability in basal draft is significantly muted in the hydrostatic calculations; for example, the southernmost feature has a height of 65 m

290   from apex to keel (blue to green dot, Fig. 3a) as measured with the IPR, but this is not seen in the hydrostatic calculations. At Site 2 the same feature can be observed, reduced to a height of 49 m from apex to keel (blue to green dot, Fig 3b). and is now visible in the hydrostatic thickness but with a height of only 20 m. The basal fractures at Site 3 are well represented in relative size and shape. By Site 3, the same basal fracture that was 65 m high 22 km up-glacier at Site 1, is 30 m high from apex to keel (blue to green dot, Fig 3c).

295

The lack of direct correspondence between basal and surface features at sites 1 and 2 precludes determining the exact vertical offset between the measured IPR thickness and ice thickness inferred from the surface elevation assuming hydrostatic equilibrium. Tidally-induced errors in the surface elevation data could cause this offset, however, tidal variation is less than a meter in this region (Padman et al, 2002) and surveys were conducted within a period of 8 days. Additionally,

300   surveys were conducted at site 3 both at the beginning and end of the data collection period and cross-over analyses did not reveal differences of more than 10 cm in surface elevation. This suggests the difference in thickness at Site 1 and 2 between measured and calculated could instead be due to bridging stresses both from the highly variable basal draft and from pinning of the ice shelf from valley walls.

305   **5 Discussion**

5.1 Complex ice morphology

The ice draft elevation DEM we present computed using REMA surface elevation data reveals complex geometry of the suture zone, with regular basal features that have different characteristics depending on which side of the suture zone they form on. Examining the REMA surface topography and using this to extrapolate the evolution of ice flow as it advects

310   downstream, it appears that the complex basal morphology is driven by fracturing on the margins of the ice shelf before it converges in the suture zone. On the Reeves Glacier side, this fracturing can be seen in the 'flame-like' features near the ice fall (see green circle in Fig. 2a). These appear to be longitudinal crevasses that occur at the grounding line as the ice begins floating at the base of the ice fall and are re-oriented in the down-flow direction. The features are not continuous and perhaps represent periods of stick-slip motion on the ice fall causing periods of enhanced fracturing and flow followed by build-up of

315   ice. These fracture features can be traced downstream to the terminus in both REMA data (Fig. 2a) and in Landsat satellite imagery (Fig. 1a).

On the northern side, the equivalent features swing away from the suture zone by almost 90º as they approach the terminus. Again, tracing these upstream, they appear to originate from fractures on the southern margin of the Priestley Glacier. The fractures take on the sweeping shape likely due to the faster speed of Reeves Glacier (~200-250 m a^{-1}) compared to Priestley

320   (~150-200 m a^{-1}), a behaviour that becomes increasingly enhanced towards the terminus. The difference in flow speed of the two portions of NIS is likely due to the pinning point of Inexpressible Island to the north (Fig. 4a). Examining the REMA elevation data for the upstream area of the NIS (as there are no *in situ* radar data in that location), the Priestly fractures first

appear with lengths of 2 km. The floating Priestly Glacier ice thins and stretches as it advects downstream towards the terminus, causing these fractures to expand laterally northwards, with lengths up to 7 km. The basal fractures on the Priestley side cause hydrostatic depressions on the surface that are easily identifiable through water ponding on the surface during the brief (<25 days per year; Bell et al, 2017) melt season of this ice shelf (Fig. 6a).

5.2 Ice shelf fractures and strain rates

There is a clear relationship between the northern flank basal fractures and the ice surface transverse strain rates (Fig. 4b,d) where extension occurs over the keels and compression over the apexes. This is likely driven by the hydrostatic balance forcing surfical bending to conform to the basal variation in ice draft, with deeper keels and shallower apexes driving the formation of hills and troughs on the ice surface, respectively. As described in Vaughan et al (2012), who applied a thin bending beam and finite element model to examine the stresses caused by variable ice shelf draft, there will be compression in the thinner ice regions and extension over the thicker ice regions.

This pattern of variable strain is stronger on the northern side potentially due to the orientation of the basal fractures relative to the flow direction of the ice (~45º) in comparison with the southern basal features, which are parallel to ice flow. Drews et al. (2015) suggested that basal channel morphology is related to the surface ice velocities on the Roi Baudouin Ice Shelf, and that surface velocities and related strain rates from satellite observation may be sufficient to characterize basal channel morphology. This seems to also be applicable to the NIS basal features and may be a useful tool when examining areas with significant variability in basal draft that might not be visible in the hydrostatic balance calculations due to bridging stresses.

The stripe of compressive strain along the suture zone center adjacent to a stripe of extensional strain on the southern side is an interesting characteristic corresponding with the thinnest region of ice. The compressive strain on the northern side is likely due to the slower speed of Priestley Glacier coupled with pinning of this ice between Inexpressible Island and the Reeves Glacier ice. On the southern side, the extensional transverse strain is due to the faster speed of the less-constrained Reeves ice compared to Priestley's. Beyond the thinnest region of the suture zone there is more extension on the southern side of the ice shelf compared to the northern side (Fig. 4d). This spatial difference in strain may contribute to the more significant lateral stretching and dampening in draft of the southern basal fractures between Site 1 and Site 3 as shown in Fig. 1c.

5.3 Ice shelf rheology

Echo-free zones in the radar records in the thinner regions of NIS (Fig. 6d) suggest the presence of accreted marine ice and/or refrozen seawater; for the purposes of this discussion we will refer to both types as "marine ice" (Holland et al., 2009). Marine ice is known to inhibit radar returns from the ice-ocean interface as it absorbs the radar signal very effectively (Moore et al, 1994). With IPR data alone we cannot assess whether these losses of signal represent full thickness rifts with refrozen seawater or as a result of frazil ice accumulation within regions of reduced ice draft. However, with the REMA hydrostatic DEM and our *in situ* survey of the ice shelf, it appears that the marine ice in the center of the suture zone originates from full-thickness fractures that refreeze with intruded ocean water at the base of Reeves Ice Fall. This is consistent with ice core analysis of marine ice frozen into a rift 7.5 km downstream of the Reeves grounding line by Khazender et al (2001). The marine ice associated with the marginal basal fractures on the Priestley side, however, may have radar signal loss because of marine ice accumulation within the fracture but not through the entire ice thickness.

Due to high surface ablation combined with basal accretion of sea water, the nearby Hell's Gate Ice Shelf (Fig. 1a) is composed entirely of marine ice (Souchez et al., 1991). This underscores that supercooled ocean water readily accumulates at the base of meteoric ice in this region. A 1.4 km transect on Hell's Gate ice shelf with our ground based radar revealed no

radar returns, which corroborates our interpretation of marine ice as the cause of echo-free zones on the NIS. The ice shelf melt map (Fig. 5a), in contrast indicates melt rates close to 1 m a^{-1} at the NIS front and freezing of marine ice within the regions of the suture zone closer to the grounding line. Similarly, generally low melt rates (0.08-0.09 m a^{-1}) are predicted for the base of the nearby, cold cavity Ross Ice Shelf, with melt increasing to 1m a^{-1} near its front (Stevens et al, 2020).

A full characterization of marine ice on the NIS would require a geophysical investigation with active seismic lines or *in situ* sampling and could elucidate useful information about cavity circulation under this ice shelf and establish whether the presence of the Terra Nova Bay polynya has an impact on basal ice accumulation. It would also allow ground truthing of the satellite melt map product

5.4 Ice shelf melt

In addition to examining regions of the NIS where mass may be accumulating in the form of marine ice, we are interested in where mass is lost. We also assess whether we are able to classify the thin ice region of the NIS at the convergence of the Priestley and Reeves glaciers as a channel or whether it is a purely ice-dynamic feature with minimal oceanic enhanced melting. Even in a cold cavity, some enhanced melt would be expected with channelized flow and, as increasing numbers of ice shelf channels are being identified (Alley et al, 2016), including many in suture zones, it is important to establish their role in alteration of the ice shelf with warming ocean waters. Alley et al (2019), who examine shear margins around the Antarctic, used the presence of polynyas to detect where the thinner ice of a suture zone has allowed enhanced oceanic flow and therefore can be classified as a channel. The NIS is associated with the substantial Terra Nova Bay polynya, a major sea ice producer in the region (Ciappa et al, 2012), which stretches the full width of the NIS. However, this is driven primarily by katabatic winds flowing over the ice shelf (Kurtz and Bromwich, 1983) and therefore we cannot use it for channelized flow classification.

At the NIS, the difference in ice thickness between the suture area (~200 m thick) and the body of the ice shelf where the floating ice initially converges (~550 m on the Priestly side, ~300 m on the Reeves side) could drive ocean current acceleration and enhanced melt. Furthermore, the change in shape of the suture zone as it advects downstream does suggest some alteration from ocean-driven melting. The thin-ice region has a longer, lower-gradient edge on the Priestly (northern) side and a steeper but shorter wall on the Reeves (southern) side, which may be due to Coriolis-forced enhanced melt towards the northern side of the channel. Coriolis-forced acceleration of currents along the flanks of channels causing enhanced melt has been identified in other basal channels around the Antarctic (Alley et al., 2016; Dutrieux et al., 2013; Gladish et al., 2012; Mankoff et al., 2012). The pinning of the Priestley ice between Inexpressible Island and the Reeves ice inhibits enhanced lateral stretching in this region, whereas the Reeves ice expands beyond lateral pinning points sooner and is therefore able to expand to the south. If driven by ice dynamics alone, it would be expected that the Reeves side of the suture zone would be the less steep flank as opposed to the Priestley. As the opposite occurs it suggests that the shape of the suture zone is altered by Coriolis-driven enhanced melt, with accelerated flow in the regions of highest basal draft driven towards the northern side of the suture zone.

We have also presented several analyses of ice shelf melt including a flux gate analysis, point analysis on the basal fracture apexes and keels (Fig. 3), and satellite-derived melt rates (Fig. 5a). Each of these techniques has limitations. The flux gate analysis, while taking account of horizontal strain, does not allow for changing ocean conditions over the >100 years for ice to advect the 22 km between Site 1 and Site 3. The point analysis is applied to basal features related to crevasses, and the initial fracturing process may have caused different size and shapes of the keels and apexes. Finally, the satellite-derived melt rates signals are close to the noise floor (uncertainty) of the dataset for the NIS and should be relied upon mainly for general patterns of melt. However, all three methods suggest that there is enhanced melt within the thinner regions of the

suture zone compared to both the keels within and at the margin of the suture zone. In particular, both the analysis of relative basal draft change and the ice shelf melt map suggest focused melt within the thinner region of the suture zone, although the melt map shows this occurs only within 12.5 km of the ice shelf terminus (Fig 5).

405   The maximum melt rate in the suture zone from the melt map is ~0.6 ± 0.5 m a^{-1}. However this rate is low compared to other ice shelves such as Getz Ice Shelf which has an area averaged melt rate of 4.15 m a^{-1} (Wei et al, 2020), and ice shelves that come into contact with relatively warm circumpolar deep water have even higher basal melt rates, such as Pine Island Glacier ice shelf (30 m a^{-1}; Dutrieux et al., 2013). Oceanographic data in Terra Nova Bay collected by Manzella et al. (1999) indicated relatively cold ocean water conditions, explaining why vertical melt rates within the suture zone are likely to be

410   small in comparison to the Amundsen Sea sector. The higher ice loss rates in the middle of the suture zone compared to the thicker edges do, however, suggest an active melt component and that the suture zone is acting to channel water.

Comparing the satellite-derived melt rates with the ocean glider data, there is a good correspondence between the locations of meltwater near Inexpressible Island and the center of Nansen Ice Shelf calving front, and the areas of enhanced melt from the ice shelf (Fig. 5a). The meltwater pulse adjacent to Inexpressible Island may originate from Priestly Glacier grounding

415   line where subglacial drainage might impact the circulation and melt rates, although given the distance between the grounding line and the observed freshwater pulse (50 km), this warrants further investigation. The meltwater observed by the glider underneath and directly offshore of the middle of the NIS calving front lines up with the region of enhanced melt within the suture zone and the thinner ice in the suture zone. However, the range of depth in the meltwater recorded by the glider means that it is hard to determine where that water originated from, although some is close to the ice draft depth of

420   150-190 m in the central region (Fig. 2c). In addition, the presence of sub-mesoscale eddies in the region near the NIS terminus may be impacting both the depth and location of the meltwater. The southernmost meltwater pulse in the ocean glider data appears to originate from Drygalski Glacier immediately adjacent to Nansen Ice Shelf.

The transverse fracture discovered in 2016 occurs at the transition into the highest melt region of the suture zone (Fig. 5a). The formation of this fracture was argued to be due to an alteration of the strain regime from transverse to longitudinal

425   extension between 2014 and 2015, linked closely to the expansion and the calving of a fracture much closer to the ice front (Dow et al, 2018). However, as this strain transition occurred in the same region as the maximum melt it is potentially linked to the higher thinning rates of this region compared to further upstream. This suggests that with ocean warming and related melt, which will also alter the draft morphology and therefore the shelf strain rates, fracturing may occur further upstream and may laterally propagate more rapidly, allowing more frequent calving events. To assess this would, however, require an

430   ocean model driven with the complex morphology that we have identified in order to determine the relative roles of supercooling and melt in the ocean cavity and how this might change over time (Goldberg et al, 2019).

5.5 Dataset applicability

With the availability of high-resolution datasets such as REMA and GoLIVE, large-scale analyses of ice shelf characteristics can be made. However, from our application of multiple data sets including *in situ* data we find that some of the ice shelf

435   properties are not well represented in the satellite-derived data sets.

The primary limitation of REMA is that hydrostatic calculations do not take into account bridging stresses and variability of ice rheology. The calculations therefore may not fully represent the ice shelf draft (Drews et al. 2015; Gladish et al., 2012; Mankoff et al., 2012; Vaughan et al., 2012). Comparing the radar data from Site 1 with the hydrostatic calculations demonstrates that not all of the basal fractures are well represented in the surface hydrostatic balance, and that there is a

440   vertical offset with hydrostatic thickness that is smaller than suggested by the radar thickness. For example, on the northern

side of the suture zone, the basal fractures in the radar are around 1600 m wide and 50 m high; this is similar to the hydrostatic balance features (which are 1655 m wide and 53 m high). On the southern side of Site 1 the features are 448 and 522 m wide with heights of 64 m and at least 82 m. Yet in the hydrostatic thickness calculations, these features are difficult to discern and have limited variability (up to 10 m). By Site 2, these features begin to be seen in the hydrostatic thickness but

445 are not fully defined. However, at Site 3, near the ice shelf front, the features on both the northern and southern sides of the central suture zone are well represented in the hydrostatic calculations. There, the same southern features are 660 and 665 m wide with heights of around 26 m. This suggests that bridging stresses are likely to obscure basal morphology only when the basal fracture features are narrow and tall; in this case narrower than ~500 m and taller than 60 m, a threshold that will likely vary with ice thickness at other ice shelves. Limited ability to detect complex ice draft geometry will inhibit applicability of

450 ocean circulation models with kilometer-scale resolution for ice shelves in the Antarctic, especially those with more active melt evolution than appears to be present at the NIS.

By comparing the REMA surface DEM and the strain rate maps, we can observe how the ice dynamics impact the ice stress conditions. However, only the transverse strain rate map provides information on the compression and extension in the keels and apexes of the basal fractures, along with the extensional and compressional striping along the suture zone. If only

455 longitudinal strain had been calculated, these features would have been missed. Given that the NIS suture zone fractures form in the Reeves extensional zone, due to its southward flow beyond the valley walls, assuming that fracture dynamics rely only on longitudinal strain (Lai et al, 2020) is not always correct.

Finally, it is challenging to determine whether suture zones and thin areas of ice shelves with complex morphology are actively melting due to channelized flow, or whether the ice thickness is due to ice dynamics alone. This is an important

460 distinction as the systems with actively melting channelized flow will be more vulnerable to warming ocean conditions potentially causing increased thinning. As the NIS transverse fractures are located in the thinnest ice regions (similar to other Antarctic ice shelves; Dow et al 2018), it demonstrates that calculations of channelized melting and ice shelf thinning are important. Here, the combination of ice flux gate analysis, the ocean glider dataset, and the satellite melt map are valuable resources for estimating ice shelf melt but are not able to provide high resolution outputs for analysis of changes in the

465 complex draft morphology of the NIS. An approach where a combination of Eulerian and Lagrangian analyses of satellite altimetry data and DEMs are used to examine spatial and temporal variability of melt (Shean et al, 2019; Chartrand and Howat, 2020) is a technique that could aid in analysis of ice shelves with complex morphology like the NIS.

6 Conclusions

The Nansen Ice Shelf is a small, cold-cavity ice shelf, yet includes a variety of complex features due to the combination of

470 ice dynamics, the shape of the embayment and interaction with the ocean. The primary causes of the complex morphology at Nansen Ice Shelf are the dynamics of upstream ice with basal fractures formed at the grounding line of Reeves Glacier and the floating margin of Priestly Glacier ice. Changes in these features as they advect downstream is evident in both the ice shelf draft and the strain rate maps, and demonstrates the competing elements of horizontal variability in transverse strain and differential ice velocities on either side of the suture zone of these two glaciers. Application of only longitudinal strain

475 rates would miss this complex relationship between the basal features and the ice strain. Although the former can provide information about controls of transverse fracture, for example, the more complex strain demonstrated by the transverse strain rates suggests that for analyses of ice shelf stability, multi-directional strain rates should be taken into account.

The basal fracturing leads to accumulation of marine ice in the full-thickness rifts associated with Reeves Glacier and in the

480 tips of basal fractures associated with Priestly Glacier, as demonstrated by radar echo-free zones and stripes of blue ice on the ice shelf surface. The combination of this variable ice rheology and significant draft variability in the upper regions of

the suture zone make application of hydrostatic calculations difficult. Comparison between ground-based radar thickness data and hydrostatic calculations suggests that bridging stresses can significantly dampen the vertical surface expression of basal draft, in this case particularly for basal features narrower than ~500 m and taller than 60 m.

485

Our analysis of changes in ice morphology, flux gate volume, oceanographic data of freshwater and satellite-derived ice shelf melt all point toward active channelized melt within the suture zone. This melt is small compared to warm cavities in the Amundsen Sea region, for instance. However, it appears to have played a role in active fracture of the NIS, with a new transverse fracture forming in 2016 in a high melt zone in the channel. The combination of the ice morphology, channelized

490 melt rate and strain patterns within the ice shelf all appear to play a role in the formation of fractures at this ice shelf, which result in large-scale, periodic calving events.

Given the key role that ice shelves play in the stability of Antarctic grounded ice, our evidence from the Nansen Ice Shelf suggests that analyses based only on satellite-derived data may miss important features of the ice shelf such as complex basal

495 morphology, the presence of marine ice, and highly variable strain patterns. As demonstrated at Nansen Ice Shelf, these factors all play a role in the dynamics of the ice shelf and the formation of fractures that can lead to large calving events.

Appendix A: Ice Penetrating Radar methods

A.1 Ground-based radar

An IceRadar (Blue Systems Integration Ltd.) equipped with 10 MHz resistively-loaded dipole antennae separated by 15 m

500 was used to collect the on-foot radar lines (Mingo and Flowers 2010). The IPR transmitter pulsed 512 times per second and the average of a stack of 50-256 traces were recorded by the receiver at an interval of 1-3 seconds.

Precise location data were simultaneously collected at 1 Hz using a Topcon Hiper V L1/L2 Global Navigation Satellite System (GNSS) receiver placed next to the IPR receiver. GNSS data were subsequently processed using Natural Resources

505 Canada's (NRCan) precise point positioning (PPP) service and corrected to the GL04C geoid datum after subtracting the height of the GNSS antenna center above the ice surface (Greene, 2021). Radar Tools (modified from release 0.4; github ID: njwilson23/irlib) was used pick the air wave and reflected wave from each trace. Ice thickness (H) was calculated as:

$$H = \sqrt{\frac{v(t+s/c)^2}{4} - \left(\frac{s}{2}\right)^2} ,$$ (A1)

where s is the antenna separation distance (15 m), t is the two-way travel time (s) from the air wave to the reflected wave, c

510 is the speed of the radar wave in air (3 x 10^8 m s^{-1}) and v is the speed of the radar wave in ice (1.68 x 10^8 m s^{-1}; Fujita et al., 2000).

A.2 Airborne radar

A radar system was installed on an Aérospatiale AS-350 helicopter in a fixed boom, and was complemented by a laser altimeter, camera, Global Positioning System (GPS), and an internal navigation system (INS) for precise positioning. Two of

515 the three fixed booms attached to the bottom of the helicopter contained separate antennae, installed in a cross-track polarized dipole arrangement, that both transmitted and received independently, with 60 MHz centre frequencies, 15 MHz chirp bandwidths, and 1 μs pulse width.

A.3 Error analysis

Where survey lines crossed, ice thickness and surface elevation values were compared at points of closest approach (within a

520 maximum distance of 20 m) to evaluate repeatability and bias between datasets. Ground-based IPR ice thickness 'crossover' points (n= 13) agreed to within 2.2 m of each other on average with a basic bootstrapped 95% confidence interval (CI) of 0.5

to 3.5 m. Crossovers from airborne IPR thickness focused on the thin ice area and ice shelf front (n = 158) agreed to within 3.3 m (CI: 2.7 to 3.9 m), whereas the general NIS survey thickness crossovers (n= 99) agreed within 7.7 m (CI: 5.6 to 9.6 m). Ice thickness in the ground-based IPR survey was 2.1 m thinner on average (n=113) than the airborne survey of the thin ice

525   area with a mean absolute difference of 3.5 m (CI: 2.8 to 4.2 m).

Average surface elevation crossover errors in the ground-based (n=23) and airborne (n=557) IPR surveys were 0.71 m (CI: 0.21 to 1.11 m) and 1.02 m (CI: 0.80 to 1.19 m), respectively. Surface elevation from ground-based surveying was 0.08 m higher on average (CI: -0.10 to 0.23 m) than the airborne elevation (n = 189) with a mean absolute difference of 0.69 m (CI: 0.54 to 0.81 m).

530   The relative uncertainty in ice shelf draft can be derived from these two errors added in quadrature. For example, NIS basal draft estimations from the ground-based survey have an uncertainty of ±3.7 m, 95% of the time, whereas the airborne survey focused on the thin region and calving front has an uncertainty of ±4.1 m; the entire airborne survey has an uncertainty of ±9.7 m.

Data availability

535   Ice penetrating radar data and locations of meltwater from the ocean glider can be found here: 10.5281/zenodo.4891281. Landsat satellite imagery is freely available from USGS (https://earthexplorer.usgs.gov/), with REMA and GoLIVE data freely available from NSIDC (https://nsidc.org). Ice shelf melt data is available through UCSD Library Digital Collections.

Author contribution

CFD and DM developed the project, analysed the radar and satellite data, and undertook the ground-based radar fieldwork.
540   PW processed the radar data and provided initial analyses. DF, ALF, and JM collected, processed, and analysed the ocean glider data. JG and DDB collected and processed the airborne radar data. CKL and WSL provided field support and contributed to project design. CFD wrote the manuscript with input from all authors.

Competing interests

The authors declare that they have no conflict of interest.

545   **Acknowledgements**

CD was supported by the Natural Sciences and Engineering Research Council of Canada (NSERC; RGPIN-03761-2017) and the Canada Research Chairs Program (950-231237). DM was supported by NSERC (RGPIN-06244-2016), the Canada Foundation for Innovation, the Ontario Research Fund (314190) and a Canadian Arctic-Antarctic exchange Polar Continental Shelf Program (647-17). Airborne radar and ocean glider data were collected by the support of the Korean
550   Ministry of Oceans and Fisheries (KIMST20190361 (PM21020), which also support W S Lee and C-K Lee. The authors also thank Jin Hong Kim for assistance in the field. This is UTIG contribution ####.

References

Adusumilli, S., Fricker, H. A., Medley, B., Padman, L., and Siegfried, M. R.: Interannual variations in meltwater input to the Southern Ocean from Antarctic ice shelves. Nat Geosci, 13(9), 616-620, 2020

555   Alley, K. E., Scambos, T. A., Siegfried, M. R., and Fricker, H. A.: Impacts of warm water on Antarctic ice shelf stability through basal channel formation. Nat Geosci, 9(4), 290-293, 2016

Alley, K. E., Scambos, T. A., Alley, R. B. and Holschuh, N.: Troughs developed in ice-stream shear margins precondition ice shelves for ocean-driven breakup. Science Advances, 5(10), p.eaax2215, 2019.

Baroni, C., Frezzotti, M., Giraudi, C., and Orombelli, G.: Ice flow and surficial velocity inferred from satellite image and air
560   photo analysis of Larsen Ice tongue, Hells Gate and Nansen ice shelves (Northern Victoria Land, Antarctica). Memorie Della Societa'Geologica Italiana, 46, 69-80. 1991

Bell, R. E., Chu, W., Kingslake, J., Das, I., Tedesco, M., Tinto, K. J., Zappa C. J., Frezzotti, M., Boghosia, A., and Lee, W. S.: Antarctic ice shelf potentially stabilized by export of meltwater in surface river. Nature, 544(7650), 344-348. 2017

Bromwich D. H. and Kurtz D. D.: Katabatic wind forcing of the Terra Nova Bay Polynya. J Geophys Res- Earth. 89(C3),
565   3561–3572, doi:10.1029/JC089iC03p03561, 1984.

Chartrand, A. M. and Howat, I. M.: Basal Channel Evolution on the Getz Ice Shelf, West Antarctica. J Geophys Res-Earth, 125(9), p.e2019JF005293, 2020.

Ciappa, A., Pietranera, L., and Budillon, G.: Observations of the Terra Nova Bay (Antarctica) polynya by MODIS ice surface temperature imagery from 2005 to 2010. Remote Sens Environ, 119, 158-172, 2012

570   Dow, C. F., Lee, W. S., Greenbaum, J. S., Greene, C. A., Blankenship, D. D., Poinar, K., Forrest, A., Young, D., and Zappa, C. J.: Basal channels drive active surface hydrology and transverse ice shelf fracture. Science Advances, 4(6), eaao7212, 2018.

Drews, R: Evolution of ice shelf channels in Antarctic ice shelves. Cryosphere, 9(3), 1169-1181, 2015.

Dupont, T. K., and Alley, R. B.: Assessment of the importance of ice-shelf buttressing to ice-sheet flow. Geophys Res Lett,
575   32(4), 2005.

Dutrieux, P., Vaughan, D. G., Corr, H. F., Jenkins, A., Holland, P. R., Joughin, I., and Fleming, A. H.: Pine Island glacier ice shelf melt distributed at kilometre scales. Cryosphere, 7(5), 1543-1555, 2013.

Frezzotti, M., Tabacco, I. E., and Zirizzotti, A.: Ice discharge of eastern Dome C drainage area, Antarctica, determined from airborne radar survey and satellite image analysis. J Glaciol, 46(153), 253-264, 2000.

580   Fricker, H. A., Popov, S., Allison, I., & Young, N.: Distribution of marine ice beneath the Amery Ice Shelf. Geophys Res Lett, 28(11), 2241-2244, 2001.

Fujita, S., Matsuoka, T., Ishida, T., Matsuoka, K., and Mae, S: A summary of the complex dielectric permittivity of ice in the megahertz range and its applications for radar sounding of polar ice sheets. In Physics of Ice Core Records (p. 185-212). Hokkaido University Press, 2000.

585   Fürst, J. J., Durand, G., Gillet-Chaulet, F., Tavard, L., Rankl, M., Braun, M. and Gagliardini, O.: The safety band of Antarctic ice shelves. Nat Clim Change, 6(5), 479-482, 2016.

Gladish, C. V., Holland, D. M., Holland, P. R., and Price, S. F.: Ice shelf basal channels in a coupled ice/ocean model. J Glaciol, 58(212), 1227-1244, 2012.

Goldberg, D. N., Gourmelen, N., Kimura, S., Millan, R. and Snow, K.: How accurately should we model ice shelf melt
590   rates? Geophys Res Lett, 46(1), 189-199, 2019.

Greene, C. Antarctic geoid conversions (https://www.mathworks.com/matlabcentral/fileexchange/54104-antarctic-geoid-conversions), MATLAB Central File Exchange. Retrieved June 2, 2021.

Holland P. R., Corr H. F., Vaughan D. G., Jenkins A, and Skvarca P: Marine ice in Larsen Ice Shelf. Geophys Res Lett, 36(11), 2009.

595   Howat I. M, Porter C, Smith B. E., Noh M. J. and Morin P.: The Reference Elevation Model of Antarctica. Cryosphere 13, 665–674, doi:10.5194/tc-13-665-2019, 2019.

Indrigo, C., Dow, C.F., Greenbaum, J.S., and Morlighem, M.: Drygalski Ice Tongue stability influenced by rift formation and ice morphology. J Glaciol, doi.org/10.1017/jog.2020.99, 2021.

600 Khazendar, A., Tison, J.L., Stenni, B., Dini, M. and Bondesan, A.: Significant marine-ice accumulation in the ablation zone beneath an Antarctic ice shelf. J Glaciol, 47(158), 359-368, 2001.

Kulessa, B., Jansen, D., Luckman, A. J., King, E. C., and Sammonds, P. R. Marine-ice regulates the future stability of a large Antarctic ice shelf. Nat Commun, 5, 3707, 2014.

Kurtz, D. D., and Bromwich, D. H. Satellite observed behavior of the Terra Nova Bay polynya. J Geophys Res - Oceans, 88(C14), 9717-9722, 1983.

605 Lai, C.Y., Kingslake, J., Wearing, M.G., Chen, P.H.C., Gentine, P., Li, H., Spergel, J.J. and van Wessem, J.M.: Vulnerability of Antarctica's ice shelves to meltwater-driven fracture. Nature, 584(7822), 574-578, 2020.

Lipovsky B.: Ice shelf rift propagation and the mechanics of wave-induced fracture. J Geophys Res – Oceans, 123, 4014–4033, doi:10.1029/2017JC013664, 2018.

Lindzey, L. E., Beem, L. H., Young, D. A., Quartini, E., Blankenship, D. D., Lee, C. K., Lee, W. S., Lee, J. I., and Lee, J.:
610 Aerogeophysical characterization of an active subglacial lake system in the David Glacier catchment,
Antarctica. Cryosphere, 14(7), 2217-2233, 2020.

Little, C.M., Gnanadesikan, A. and Oppenheimer, M.: How ice shelf morphology controls basal melting. J Geophys Res - Oceans, 114(C12), 2009.

615 Mankoff, K. D., Jacobs, S. S., Tulaczyk, S. M., and Stammerjohn, S. E.: The role of Pine Island Glacier ice shelf basal channels in deep-water upwelling, polynyas and ocean circulation in Pine Island Bay, Antarctica. Ann Glaciol, 53(60), 123-128, 2012.

Manzella, G. M. R., Meloni, R., and Picco, P.: Current, temperature and salinity observations in the Terra Nova Bay polynya area. In Oceanography of the Ross Sea Antarctica (pp. 165-173). Springer, Milano, 1999.

620 Mingo, L. and Flowers, G.E.: An integrated lightweight ice-penetrating radar system. J Glaciol, 56(198), 709-714, 2010.

Moore, J. C., Reid, A. P., and Kipfstuhl, J.: Microstructure and electrical properties of marine-ice and its relationship to meteoric ice and sea ice. J Geophys Res - Oceans, 99(C3), 5171-5180, 1994.

Mouginot, J., B. Scheuchl, and E. Rignot.: MEaSUREs Antarctic Boundaries for IPY 2007-2009 from Satellite Radar, Version 2. Boulder, Colorado USA. NASA National Snow and Ice Data Center Distributed Active Archive Center.
625 doi:10.5067/AXE4121732AD, 2017

Padman, L., Fricker, H. A., Coleman, R., Howard, S., and Erofeeva, L.: A new tide model for the Antarctic ice shelves and seas. Ann Glaciol, 34, 247-254, 2002.

Rusciano, E., Budillon, G., Fusco, G., and Spezie, G.: Evidence of atmosphere–sea ice–ocean coupling in the Terra Nova Bay polynya (Ross Sea—Antarctica), Cont Shelf Res, 61–62, 112–124, doi:10.1016/j.csr.2013.04.002, 2013

630 Shean, D. E., Joughin, I. R., Dutrieux, P., Smith, B. E. and Berthier, E.: Ice shelf basal melt rates from a high-resolution digital elevation model (DEM) record for Pine Island Glacier, Antarctica. Cryosphere, 13(10), 2633-2656, 2019.

Scambos, T. A., Berthier, E., Haran, T., Shuman, C. A., Cook, A. J., Ligtenberg, S., and Bohlander, J.: Detailed ice loss pattern in the northern Antarctic Peninsula: widespread decline driven by ice front retreats. Cryosphere, 8(6), 2135-2145, 2014.

635 Scambos, T., Fahnestock, M., Moon, T., Gardner, A., and Klinger, M.: Global Land Ice Velocity Extraction from Landsat 8 (GoLIVE), Version 1. Boulder, Colorado USA. NSIDC: National Snow and Ice Data Center. doi:10.7265/N5ZP442B, 2016.

Souchez, R., Meneghel, M., Tison, J. L., Lorrain, R., Ronveaux, D., Baroni, C., Lozej, A., Tobacco, I., and Jouzel, J.: Ice composition evidence of marine-ice transfer along the bottom of a small Antarctic ice shelf. Geophys Res Lett, 18(5), 849-852, 1991

640   Stevens, C., Lee, W. S., Fusco, G., Yun, S., Grant, B., Robinson, N., and Hwang, C. Y.: The influence of the Drygalski Ice Tongue on the local ocean. Ann Glaciol, 58(74), 1–9, doi:10.1017/aog.2017.4, 2017.

Stevens, C., Hulbe, C., Brewer, M., Stewart, C., Robinson, N., Ohneiser, C. and Jendersie, S.: Ocean mixing and heat transport processes observed under the Ross Ice Shelf control its basal melting. P Natl Acad Sci, 117(29), 16799-16804, 2020.

645   Wei, W., Blankenship, D. D., Greenbaum, J. S., Gourmelen, N., Dow, C. F., Richter, T. G., ... and Assmann, K. M.: Getz Ice Shelf melt enhanced by freshwater discharge from beneath the West Antarctic Ice Sheet. Cryosphere, 14(4), 1399-1408, 2020.

Weertman, J. Can a water-filled crevasse reach the bottom surface of a glacier. International Association of Hydrological Sciences, 95, 139-145, 1973.

650   Vaughan, D. G., Corr, H. F., Bindschadler, R. A., Dutrieux, P., Gudmundsson, G. H., Jenkins, A., Newman, T., Vornberger, P., and Wingham, D. J.: Subglacial melt channels and fracture in the floating part of Pine Island Glacier, Antarctica. J Geophys Res - Earth, 117(F3), 2012.

Yoon, S.-T., Lee, W. S., Stevens, C., Jendersie, S., Nam, S., Yun, S., Hwang, Y., Jang, G. I., and Lee, J.: Variability in high-salinity shelf water production in the Terra Nova Bay polynya, Antarctica, Ocean Sci, 16, 2020.

655